## A Guide To Power Electronics Design For Off-Battery Automotive (Part 4): DC-DC Conversion From 400 V

*by Timothy Hegarty, Texas Instruments, Phoenix, Ariz.*

Earlier parts of this series[1-3] discussed requirements and dc-dc converter designs for powering embedded automotive applications in conventional vehicles with 12-V or 24-V buses and in mild hybrid vehicles with 48-V buses. However, new power conversion requirements have emerged in electric vehicle (EV) subsystems with higher voltage levels and increased complexity. Take, for example, a battery electric vehicle (BEV) with a nominal battery voltage of 400 V or 800 V and a plug-in hybrid electric vehicle (PHEV) with a nominal battery voltage of 300 V.

With higher-capacity battery packs enabling longer range capability, wider access to fast-charging infrastructures, and an overall cost-of-ownership reduction—not to mention the price volatility and security of fossil-fuel supplies—customer demand for EVs continues to increase,[4] displacing internal combustion engine (ICE) vehicles. Impressive EV market growth comes alongside sustained government efforts to accelerate decarbonization, with a growing number of countries pledging to phase out ICE vehicles completely, or setting ambitious vehicle electrification targets for the coming decade.

The main development challenge with BEVs and PHEVs is to implement an ultra-efficient electric or hybrid-electric powertrain to maximize vehicle range. And while most headlines related to EVs focus on battery-system innovations, advancements in power electronics can push EV performance envelopes even further.[5] At the heart of every BEV and PHEV are several power electronics subsystems: a traction inverter, onboard charger, dc-dc converter and battery management system (BMS), as shown in Fig. 1. Two voltage domains exist, based on a high-voltage battery pack for traction and a low-voltage auxiliary battery to supply legacy vehicle loads such as body electronics, lighting and infotainment.
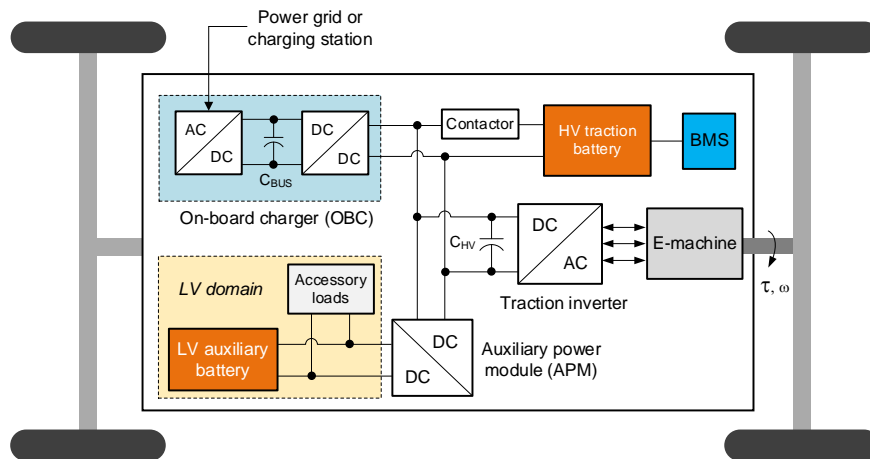


*Fig. 1. BEV/PHEV dual-battery architecture with several high-voltage subsystems and an electric drive system. The auxiliary power module (APM) provides dc-dc conversion between the high-voltage battery pack and the low-voltage battery. This traction-to-auxiliary dc-dc converter acts as an "electric alternator," delivering power levels up to 5 kW.*

The load current requirements on the low-voltage side continue to increase, underpinned by the conversion of mechanical components to electrical functions[3] for increased performance and the advent of autonomous self-driving systems. Whereas an ICE vehicle uses a belt-driven alternator to charge the low-voltage battery, a BEV or PHEV uses an auxiliary power module (APM) for dc-dc conversion between the high-voltage battery pack and the low-voltage battery. This traction-to-auxiliary (T2A) dc-dc converter operates continuously during vehicle use and behaves effectively as an "electric alternator," with power levels up to 5 kW.

In some cases, energy needs to transfer from the low-voltage side to the high-voltage side, thus requiring a topology capable of bidirectional power flow. More important, the interface between the high- and low-voltage domains must provide galvanic isolation to protect the low-voltage system from potential hazards, especially because the return connection on the low-voltage side is the vehicle's chassis.

This article charts several steps within the context of designing a dc-dc power stage with a high conversion ratio for an APM subsystem. The steps include reviewing the applicable standards and functional safety requirements; collating a list of circuit specifications; assessing the need for bidirectional power flow and choosing a suitable topology and control scheme; generating a schematic and bill of materials; understanding the design considerations for the control architecture and magnetic components; and finally, completing functional validation and performance evaluation.

### Applicable Standards

Table 1 lists several standards[5-10] pertaining to high-voltage components in BEV and PHEV designs. This includes CISPR 12, CISPR 25 and CISPR 36 for conducted and radiated electromagnetic interference (EMI), ISO 7637-4 for conducted immunity, ISO 6469-3 for electrical safety, and ISO 21948-2 for tests and procedures specifically related to high-voltage components. UNECE Regulation No. 100 is a European regulatory requirement for EVs—part 1 in particular describes specific requirements for the electric powertrain, primarily related to the prevention of electric shock.

Table 1. Relevant standards for high-voltage systems in EVs.

| Standard | Edition | Year | Title |
|---|---|---|---|
| CISPR 25 | 5 | 2021 | Vehicles, boats and internal combustion engines – Radio disturbance characteristics – Limits and methods of measurement for the protection of on-board receivers |
| CISPR 12 | 6 | 2007 | Vehicles, boats and internal combustion engines – Radio disturbance characteristics – Limits and methods of measurement for the protection of off-board receivers |
| CISPR 36 | 1 | 2020 | Electric and hybrid electric road vehicles – Radio disturbance characteristics – Limits and methods of measurement for the protection of off-board receivers below 30 MHz |
| IEC 61000-6-3 | 3 | 2020 | Electromagnetic compatibility (EMC) – Part 6-3: Generic standards – Emission standard for equipment in residential environments |
| ISO 21948-2 | 1 | 2021 | Electrically propelled road vehicles – Electrical specifications and tests for voltage class B systems and components – Part 2: Electrical tests for components |
| ISO 7637-4 | 1 | 2020 | Road vehicles – Electrical disturbance by conduction and coupling – Part 4: Electrical transient conduction along shielded high voltage supply lines only |
| ISO 6469-3 | 4 | 2021 | Electrically propelled road vehicles – Safety specifications – Part 3: Electrical safety |
| UNECE Reg 100 | 3 | 2021 | Uniform provisions concerning the approval of vehicles with regard to specific requirements for the electric power train |
| ISO 26262 | – | 2018 | Functional safety series of standards (parts 1 to 12) |

The "big five" German automotive manufacturers (Audi, BMW, Daimler, Porsche and Volkswagen) use LV 123 to define relevant electrical requirements and test procedures for high-voltage automotive systems. This is a unified document based on manufacturer internal standards, such as Volkswagen VW 80303, BMW GS 95023 and Mercedes MBN LV 123. However, ISO 21498-2, a standard published in 2021 that's similar to LV 123 and now supported by all original equipment manufacturers (OEMs), covers tests for electrical and electronic components at voltage class B used for electrically propelled road vehicles. Here, class B refers to working voltages between 60 V dc and 1,500 V dc.

CISPR 36, which applies to vehicles with a traction battery voltage between 100 V and 1,000 V, was released in 2020 and applies to radiated emissions in the frequency range of 150 kHz to 30 MHz. CISPR 36 is relevant because vehicles with electric propulsion tend to produce radiated EMI in lower frequency bands that are not covered by CISPR 12 (a standard also for the protection of offboard receivers, but in the frequency range of 30 MHz to 1 GHz).

CISPR 36 describes tests to measure the magnetic field emissions (in units of dBµA/m) produced on all sides of an EV. And although the emissions are measured at a 3-m test distance, the limits as derived allow protection of offboard receivers at a 10-m separation distance, similar to CISPR 12.

Meanwhile, CISPR 25 covers the protection of receivers used onboard the same vehicle as the disturbance source(s), and limits both conducted and radiated emissions. Finally, the IEC 61000-6-3 generic emissions standard can apply in addition to the CISPR 12, 25 and 32 product family standards.

## Functional Safety

The development and integration of automotive functionalities reinforces the need for functional safety and for evidence that functional safety objectives are satisfied. Unlike traditional safety concerns related to electrical shock or fire, the functional safety process seeks to prevent or mitigate hazards that may occur if a system malfunctions.

Officially released in 2011 as an adaptation of IEC 61508 and now published as 12 individual parts, the ISO 26262 series of functional safety standards addresses sector-specific needs of electrical and electronic systems within road vehicles. For example, parts 4, 5 and 6 of ISO 26262 consider product development at the system, hardware and software levels, respectively; part 8 considers hardware element classes (supporting processes); part 9 considers Automotive Safety Integrity Level (ASIL)- and safety-oriented analyses; and part 11 details requirements for semiconductors.

Given the increasing risks from systematic failures and random hardware failures in EVs, ISO 26262 becomes an absolute necessity, with ASIL A and ASIL D representing the least and most stringent levels of risk reduction, respectively. Designers determine an ASIL rating by performing a risk analysis of potential hazards based on three key variables: severity (S), probability of exposure (E) and controllability (C) by the driver.[11] The ASIL classification then translates to the system architecture as safety goals.

Considering the dc-dc converter (APM) subsystem is a defining factor for the safety of EVs; certification to at least an ASIL C level is also becoming a market need for APMs. The system solution detailed in the remainder of this article is based on a reference design[12] assessed and classified by a third party, TÜV SÜD, to meet a systematic capability up to ASIL D.

## System Solution

### Circuit Specifications

Table 2 outlines a typical set of specifications for an APM subsystem. The high-voltage side requires overvoltage protection (OVP), undervoltage protection (UVP) and inrush current control, whereas the low-voltage side needs OVP, overcurrent protection (OCP) and short-circuit protection (SCP).

Table 2. Specifications for a bidirectional dc-dc regulator.

| Design parameter | | Specification |
|---|---|---|
| Traction battery (Li-ion) | Voltage (nominal) | 400 V |
| | Voltage range (steady state) | 250 V to 450 V |
| | Current (maximum) | 20 A |
| Auxiliary battery (Li-ion or lead acid) | Voltage (nominal) | 12 V |
| | Voltage range (steady state) | 10 V to 15 V |
| | Current (maximum) | 300 A |
| | Power (maximum) | 3.6 kW (buck mode); 100 W (boost mode) |
| Performance | Efficiency | >95%, buck mode |
| | Power-flow direction | Bidirectional |
| | Isolation barrier | Reinforced insulation, 2.75 kV |
| | Load transient response – low-voltage side | 5% to 100% load step with voltage deviation <5% |
| Functional evaluation | High-voltage electrical tests and procedures | ISO 21948-2, LV 123 |
| Protections | High-voltage side | OVP, UVP, inrush current |
| | Low-voltage side | OVP, OCP, SCP |
| Standards | Emissions | CISPR 25 Class 5 (system- and vehicle-level tests) |
| | | CISPR 12, CISPR 36 (vehicle-level tests) |
| | Immunity | ISO 7637-4, ISO 11452 |
| | Safety | ISO 6469-3, UNECE Reg. 100 |
| | Functional safety | ISO 26262 ASIL D |

## Bidirectional Capability

Located on the dc link between the high-voltage battery and the traction inverter, a bank of aluminum electrolytic capacitors, designated as $C_{HV}$ in Fig. 1, is essential to suppress inverter ripple currents. For functional safety when the vehicle is in idle mode, a dedicated relay or contactor disconnects the high-voltage battery pack from the capacitor bank, allowing active discharge of the bus capacitance.

When the EV starts operating, the dc-dc converter precharges $C_{HV}$ to the high-voltage battery's voltage level using a step-up conversion from the low-voltage battery, thus eliminating an inefficient and expensive pre-

charging circuit. The contactor then closes, and the dc-dc regulator delivers energy in the forward path with high- to low-voltage stepdown conversion.

Bidirectional operation of the APM does not need to be fully symmetrical—the reverse power flow required for capacitor pre-charge during startup is less than 100 W, much lower than that specified in the forward direction. Analog controllers are popular for unidirectional power transfer. However, digital control using a microcontroller (MCU) is most convenient when bidirectional capability is required.

## Topology

Table 3 provides relevant details about the power-stage topology and control structure related to the solution described in this article. The solution leverages Texas Instruments' "ASIL D Safety Concept-Assessed High-Speed Traction, Bidirectional DC/DC Conversion Reference Design"[12] and "Automotive 400-V Battery to 12-V, 3.6 kW DC/DC Converter Reference Design,"[13] which describe an enhanced phase-shift full-bridge (PSFB) topology using digital and analog control, respectively.

The power stage, voltage and current sensing, and control implementation in the ASIL D reference design enable bidirectional operation, and the host MCU runs a digital control loop for flexibility to manage the direction of power flow. Of course, the emphasis is on optimization of the forward (high-voltage to low-voltage) path given the higher power requirement. However, the PSFB topology operates in the reverse direction for a short duration, effectively as a current-fed push-pull circuit on the low-voltage side, with full-bridge rectification on the high-voltage side.

Table 3. Topology and control details for a bidirectional dc-dc regulator.

| Parameter | | Notes | |
|---|---|---|---|
| Topology | Primary side | PSFB with SiC MOSFETs and isolated half-bridge gate drivers | |
| | Secondary side | Current-doubler rectifier; paralleled silicon MOSFETs with low-side gate drivers; multiple synchronous rectification schemes for optimized light-load efficiency | |
| Control | Switching frequency | 100-kHz fixed | |
| | Control architecture | Digital peak current-mode control with slope compensation | |
| | Current sensing | Primary ac current | Current-sense transformer |
| | | Low-voltage port dc bus current | Paralleled shunt resistors |
| | Voltage sensing | High-voltage port dc bus voltage | Resistor divider with isolation amplifier |
| | | Low-voltage port dc bus voltage | Resistor divider |
| | MCUs | TMS320F28388 – host MCU | |
| | | TMS570 – safety monitor MCU | |
| | Control-stage integration | APM and traction inverter subsystems share both host and safety MCUs | |

Fig. 2 is a schematic of the dc-dc power stage. A high current delivered to the low-voltage side is possible with a single-winding secondary, a current-doubler synchronous rectifier and a magnetically coupled structure for the secondary-side filter inductor.
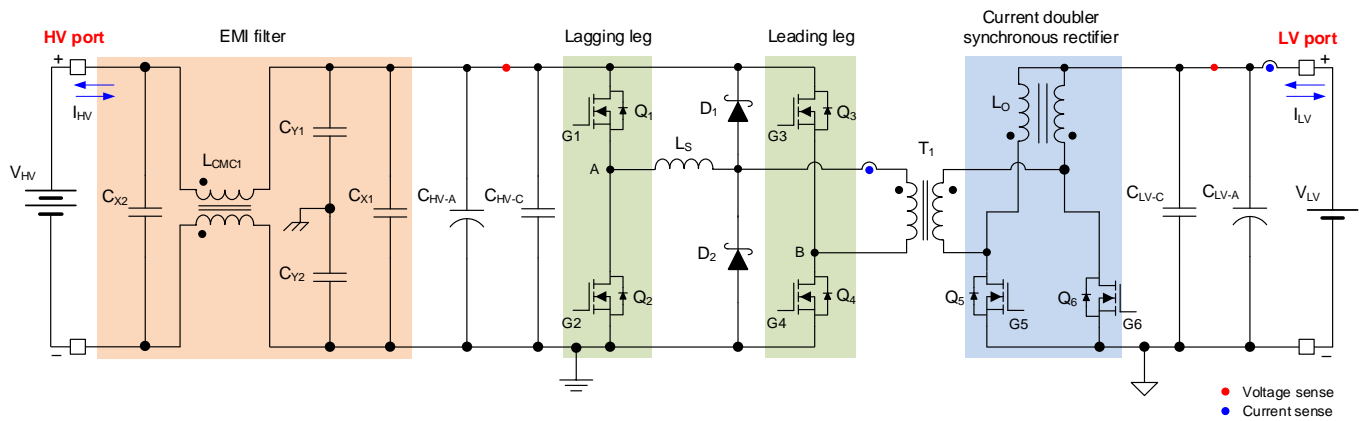
*Fig. 2. Schematic of the dc-dc power stage with an enhanced PSFB topology and current-doubler synchronous rectifier.*

The PSFB regulator is often used for EV applications given its attractive characteristics, such as a fixed switching frequency and wide-range zero-voltage switching (ZVS) or low-voltage switching (LVS) of the primary-side MOSFETs.[14, 15] ZVS and LVS reduce voltage slew rates, switching losses and EMI. Being a buck-derived topology, the PSFB has a simple input-to-output conversion law that enables a wide-voltage conversion range. To illustrate converter operation, Figs. 3 and 4 provide simulated primary- and secondary-side waveforms, respectively, at nominal battery voltages of 400 V and 12 V.

Each full-bridge MOSFET in Fig. 2 turns on for slightly less than half of a switching period. A phase shift ϕ between the control signals of the two full-bridge legs (designated as lagging and leading legs in Fig. 2) adjusts the duty cycle of the voltage applied to the transformer. Energy transfers occur with phase-shift control when diagonal MOSFET pairs $Q_1$ and $Q_4$ or $Q_2$ and $Q_3$ conduct. As the control level increases, a corresponding increase of phase shift and MOSFET conduction overlap occurs, leading to four main operating states in each switching period: two powering and two freewheeling.
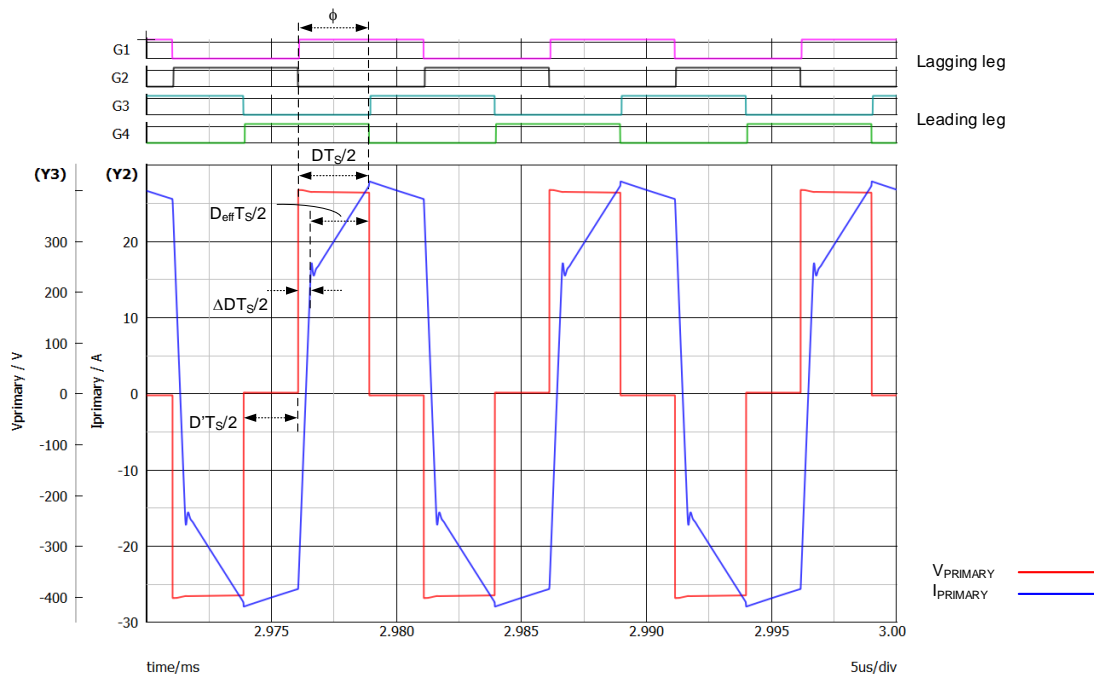


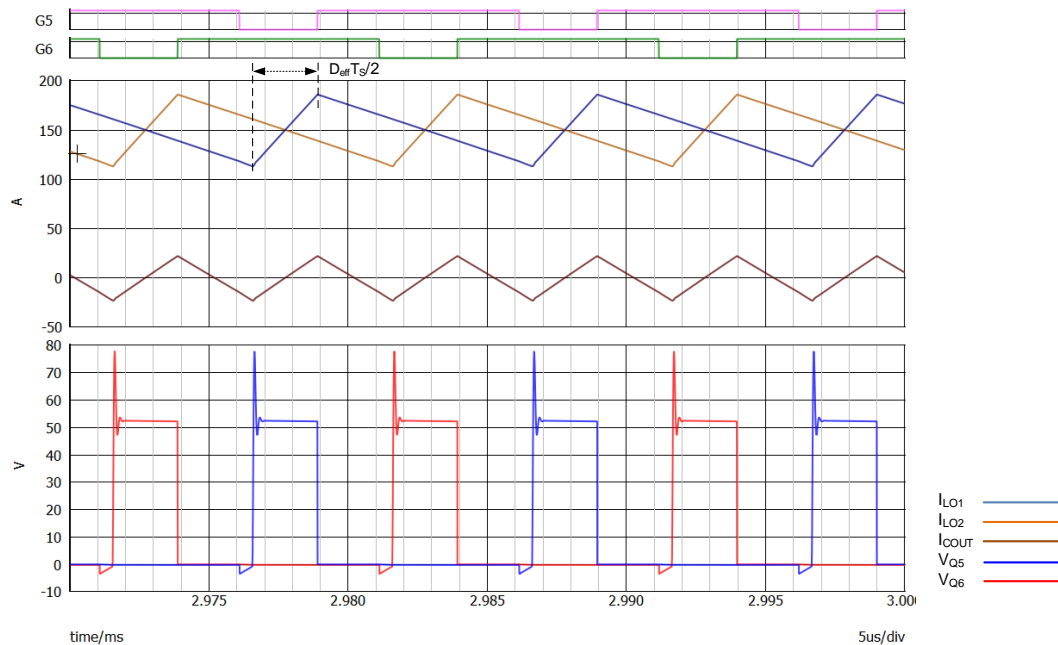*Fig. 3. Primary-side waveforms: gate-drive signals, primary voltage and primary current.*

*Fig. 4. Secondary-side waveforms: gate-drive signals, filter inductor and capacitor currents, and synchronous rectifier MOSFET drain voltages.*

The secondary-side filter inductors supply the load current during the freewheeling states when the transformer is short-circuited by either the high-side MOSFETs $Q_1$ and $Q_3$, or the low-side MOSFETs $Q_2$ and $Q_4$. This short circuit is the key difference between the PSFB and a conventional hard-switched full bridge—it prevents the magnetizing current from decaying to zero, which results in available energy to drive ZVS transitions.

Digital control facilitates adaptive dead time as a function of load current[16] to optimize ZVS at light loads. Furthermore, optional clamping diodes, designated $D_1$ and $D_2$ in Fig. 2, suppress the synchronous rectifier MOSFET drain-to-source voltage ringing on the secondary side and increase the commutating energy for lagging-leg ZVS.[17]

On the secondary side, the current-doubler synchronous rectifier shown in Fig. 2 is optimized for high-current applications. Unlike a center-tapped rectifier with two secondary windings, the current-doubler arrangement splits the current between two filter inductors, which reduces conduction losses and improves thermal distribution, in addition to the ripple cancellation and frequency-doubling effect in the capacitors. Fig. 2 shows the two inductors integrated into one coupled-inductor structure.[18]

A shim inductance, $L_S$, adds to the transformer leakage inductance to increase the load range over which ZVS applies for the lagging leg. However, while more stored inductive energy is available for light-load ZVS, the passive-to-active transition (from freewheeling to powered states) has increased the current commutation time, as suggested by equation 1, which leads to a loss of duty cycle (given by ΔD in equation 2):

$$\left| \frac{di_{pri}}{dt} \right| = \frac{V_{IN}}{L_S} \qquad (1)$$

If $D_{eff}$ is the effective duty cycle that relates to the voltage gain of the converter, the effective on-time is $D_{eff}T_S/2$, as shown in Figs. 3 and 4, where $T_S$ is the switching period. Equation 2 gives the actual duty cycle that includes ΔD and $D_{eff}$:

$$D = D_{eff} + \Delta D \approx \frac{2 \cdot V_{LV} \cdot N_1}{V_{HV}} + \frac{2 \cdot L_S \cdot F_{SW} \cdot (I_{LV}/2)}{N_1 \cdot V_{HV}} \qquad (2)$$

where $N_1$ is the transformer turns ratio.

Equation 3 gives the output voltage of the PSFB as:

$$V_{LV} = \frac{D_{eff} \cdot V_{HV}}{2 \cdot N_1} - \frac{L_S \cdot F_{SW} \cdot I_{LV}}{N_1^2} \qquad (3)$$

## Control And Safety MCUs

The integration of multiple powertrain subsystems[19, 20] is possible from a control standpoint by availing of a single host MCU with high real-time control performance to accomplish all control-related tasks. In this example, a TMS320F28388D MCU controls the APM and also an adjacent traction inverter subsystem. A TMS570 MCU provides safety-related functions. See the block diagram in Fig. 5 for more detail.[12] Both MCUs are referenced to the low-voltage-side ground, with an isolated gate drive and sensing to interface across to the high-voltage side.
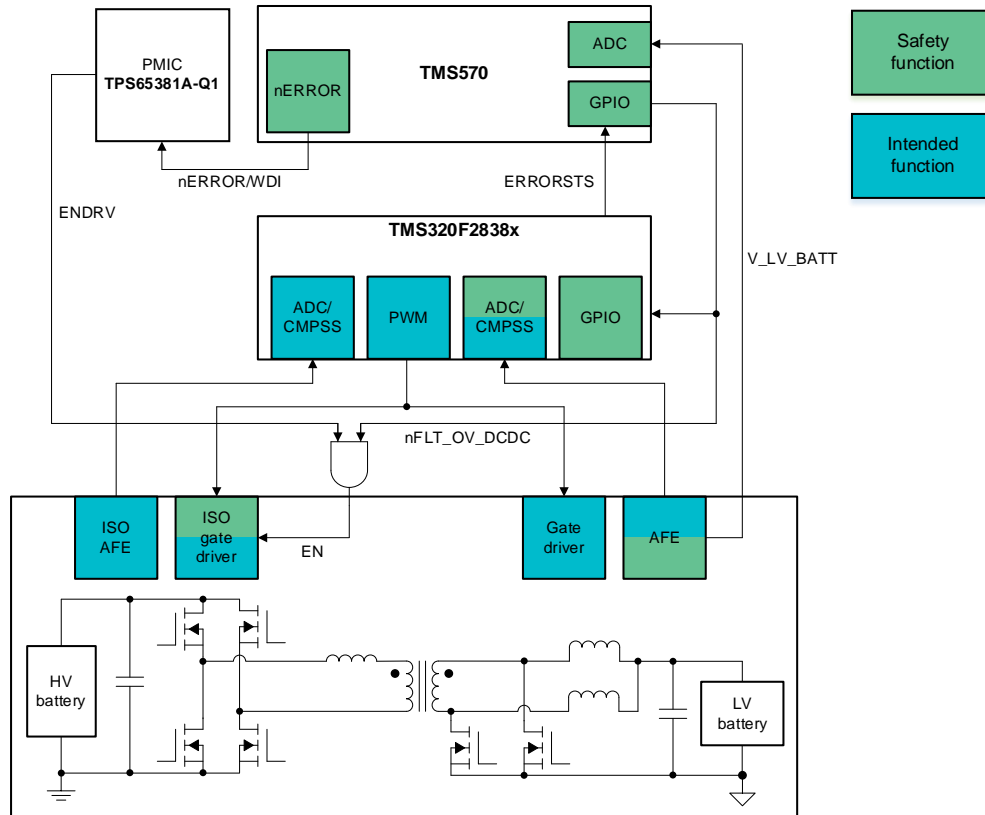


*Fig. 5. Block diagram of the APM with control and safety MCUs.*

The host MCU generates six gate signals: four for the full-bridge SiC MOSFETs (passed through isolated gate drivers) and two for the synchronous rectifier silicon MOSFETs. The MCU runs a digital peak current-mode control loop to achieve voltage and current regulation, adaptive PWM timing delays for ZVS, primary-side cycle-by-cycle peak current limiting, and transformer flux balancing (obviating the need for a dc blocking capacitor in series with the primary winding).

TI's UCC21530-Q1 isolated half-bridge gate driver supports an enable function that allows the safety MCU to disable the power stage independent of the gate signals from the MCU. The gate-driver isolated power supply has a second layer of enable for redundancy.

## Components

Table 4 details the main bill-of-materials components of the dc-dc power stage, with reference designators according to the schematic of Fig. 2. The full bridge uses SiC MOSFETs and clamping diodes. Table 5 gives a list of the main ICs in the design.

Table 4. Bill-of-materials components for the PSFB power stage.

| Ref. Des. | Component | Vendor | Part number | Description | Size (mm) |
|---|---|---|---|---|---|
| $Q_1$, $Q_3$ | High-side SiC FET (2) | Wolfspeed | C3M0065100K | 1 kV, 35 A, 65 mΩ, 37 nC, TO247-4 | 23.45 × 16 × 5 |
| $Q_2$, $Q_4$ | Low-side SiC FET (2) | | | | |
| $D_1$, $D_2$ | SiC Schottky diode (2) | Wolfspeed | C6D10065A | 650 V, 10 A, TO220-2 | 18 × 10 × 4.4 |
| $Q_5$, $Q_6$ | Synchronous rectifier MOSFET (8) | Infineon | IPP120N08S4-03 | 80 V, 2.4 mΩ, 128 nC, TO220-3 | 17 × 10 × 4.4 |
| $L_S$ | Shim inductor | Coilcraft | SER2915H-472KL | 4.7 µH, 1.86 mΩ, 20 A | 28 × 28 × 15.3 |
| $L_O$ | Coupled inductor | Cyntec | VI-19158A | 3.1 µH × 2, 0.17 mΩ, 200 A | 47 × 39 × 42 |
| $T_1$ | Main transformer | Cyntec | VT-19151B | $L_{MAG(min)}$ 500 µH, $V_{ISO}$ 5 kV, $L_{LK}$ 1.9 µH | 94.5 × 66 × 42 |
| $T_2$ | Current-sense transformer | Coilcraft | CST2010-100LB | 8 mH, 40 A, 100-to-1 | 20 × 14.5 × 10 |
| $C_{LV-C}$ | Ceramic capacitor (6) | Murata | GRM32ER7YA106K | 10 µF, 35 V, X7R, 1210 | 3.2 × 2.5 × 2.7 |
| $C_{LV-A}$ | Aluminum electrolytic capacitor (4) | TDK | B41896C7397M000 | 390 µF, 35 V, 61 mΩ | 12.5 ϕ × 20 |
| $C_{HV-C}$ | Ceramic capacitor (4) | Knowles | 2220Y6300105KXT | 1 µF, 630 V, X7R, 2220 | 5.7 × 5 × 4.5 |
| $C_{HV-A}$ | Aluminum electrolytic capacitor (2) | Nichicon | LGN2X121MELC35 | 120 µF, 600 V, 0.74 Arms | 35 ϕ × 35 |
| $C_X$ | X-capacitor | TDK | LGN2X121MELC35 | 10 µF, 630 V, X2, film | 42 × 28 × 42.5 |
| $C_Y$ | Y-capacitor (2) | Murata | DE6E3KJ222MN3A | 2.2 nF, 300 Vac, Y2 | 9 ϕ × 7 |
| $L_{CMC1}$ | Common-mode choke | Würth | 7448052502 | 2.5 mH, 25 A, 2.2 mΩ | 36 × 23 × 34 |

Table 5. Integrated circuits (all from TI) for gate drivers, controllers, bias power and MCUs.

| Ref. Des. | Component | Part number | Description | Size (mm) |
|---|---|---|---|---|
| $U_1$ | Dual-channel SiC FET isolated gate driver (2) | UCC21530-Q1 | Gate driver, 4 A/6 A, SOIC-14 | 10.3 × 10.3 × 2.65 |
| $U_2$ | Dual-channel low-side FET gate driver (4) | UCC27524A-Q1 | Gate driver, 5 A, SOIC-8 | 4.9 × 6 ×1.75 |
| $U_3$ | Isolated gate driver bias supply (2) | LM5181-Q1 | Primary-side regulated flyback converter, WSON-8; 15-V and −4-V dual output | 4 × 4 × 0.8 |
| $U_4$ | Control (host) MCU | TMS320F28388D | C2000 32-bit real-time MCU, LQFP-176 | 24 × 24 × 1.6 |
| $U_5$ | Safety monitor MCU | TMS570 | MCU for functional safety applications, LQFP-144 | 22 × 22 × 1.4 |

## Magnetics

Equation 4 estimates the transformer's primary-secondary turns ratio, $N_1$, based on a 90% maximum effective duty cycle (referred to a half-switching period) at the minimum high-voltage and maximum low-voltage battery voltages specified in Table 1:

$$N_1 = \frac{D_{eff\text{-}max}}{2} \cdot \frac{V_{HV(min)} - 2 \cdot V_{DS(pri)}}{V_{LV(max)} + V_{DS(SR)}} = \frac{0.9}{2} \cdot \frac{(250\,V - 2 \cdot 1.4\,V)}{(15\,V + 0.2\,V)} \approx 7.3 \qquad (4)$$

where the voltage drops of the primary- and secondary-side MOSFETs at full load are 1.4 V and 0.2 V, respectively.

Choosing a turns ratio of 7-to-1, equation 5 gives the duty cycle at nominal battery voltages of 400 V and 12 V as

$$D_{eff} = 2 \cdot \frac{N_1 \cdot (V_{LV} + V_{DS(SR)})}{V_{HV(min)} - 2 \cdot V_{DS(pri)}} = 2 \cdot \frac{7 \cdot (12\,V + 0.2\,V)}{400\,V - 2 \cdot 1.4\,V} = 0.43 \qquad (5)$$

With a current-doubler arrangement on the secondary side, each filter inductor sees half the output current and switching-frequency ripple current. Equation 6 finds a value for the filter inductances, assuming 50% ripple current in each inductor at nominal battery voltages:

$$L_O = \frac{(V_{LV(max)} + V_{DS(SR)}) \cdot (1 - D_{eff}/2)}{\Delta I_{Lo} \cdot F_{SW}} = \frac{(12\,V + 0.2\,V) \cdot (1 - 0.43/2)}{0.5 \cdot \dfrac{300\,A}{2} \cdot 100\,kHz} = 1.28\ \mu H \qquad (6)$$

A coupled inductor, each winding with two turns and an inductance of 1.3 µH, conveniently meets this requirement using one magnetic structure.

The duty cycle loss at full load from equation 2 is approximately 5.4% at the nominal high-voltage battery voltage. Equation 7 gives the primary-referred nominal and maximum duty cycles corresponding to the nominal and minimum high-voltage battery voltages, respectively:

$$D = D_{eff} + \Delta D \approx \frac{2 \cdot N_1 \cdot V_{LV}}{V_{HV}} + \frac{2 \cdot (I_{LV}/2) \cdot L_S \cdot F_{SW}}{N_1 \cdot V_{IN}}$$

$$D_{nom} = \frac{2 \cdot 7 \cdot 12\,V}{400\,V} + \frac{300\,A \cdot 5\,\mu H \cdot 100\,kHz}{7 \cdot 400\,V} = 0.43 + 0.054 = 0.49 \tag{7}$$

$$D_{max} = \frac{2 \cdot 7 \cdot 15\,V}{250\,V} + \frac{300\,A \cdot 5\,\mu H \cdot 100\,kHz}{7 \cdot 250\,V} = 0.84 + 0.086 = 0.93$$

If the transformer magnetizing inductance, $L_{MAG}$, is too low, a high magnetizing current ramp could cause the regulator to exhibit voltage-mode control behavior instead of peak current-mode control (the magnetizing current effectively acting as a PWM ramp, swamping out the current-sense signal). Use equation 8 to derive a minimum value for $L_{MAG}$, assuming that the magnetizing current is equal to one-quarter the reflected ripple current at the maximum input voltage:

$$L_{MAG} \geq \frac{V_{HV} \cdot D_{eff}}{\frac{\Delta I_{Lo}}{4 \cdot N_1} \cdot 2 \cdot F_{SW}} = \frac{400\,V \cdot 0.43}{\frac{75\,A}{4 \cdot 7} \cdot 2 \cdot 100\,kHz} = 330\,\mu H \tag{8}$$

Choosing 500 µH as the magnetizing inductance, equation 9 gives the peak-to-peak magnetizing current as:

$$\Delta I_{LMAG} = \frac{V_{HV} \cdot D_{eff}}{L_{MAG} \cdot 2 \cdot F_{SW}} = \frac{400\,V \cdot 0.43}{500\,\mu H \cdot 2 \cdot 100\,kHz} = 1.72\,A \tag{9}$$

Equations 10 and 11 calculate the peak and valley currents in the primary and secondary windings as:

$$I_{PRI-peak} = \frac{1}{N_1} \cdot \left( \frac{I_{LV} + \Delta I_{Lo}}{2} \right) + \frac{\Delta I_{LMAG}}{2} = \frac{1}{7} \cdot \left( \frac{300\,A + 75\,A}{2} \right) + \frac{1.72\,A}{2} = 27.7\,A$$

$$I_{PRI-valley} = I_{PRI-peak} - \frac{\Delta I_{Lo}}{N_1} - \Delta I_{LMAG} = 27.7\,A - \frac{75\,A}{7} - 1.72\,A = 15.3\,A \tag{10}$$

$$I_{PRI-valley2} = I_{PRI-peak} - \frac{V_{LV} \cdot N_1}{L_O \cdot N_1^2 + L_S} \cdot \frac{1 - D}{2 \cdot F_{SW}}$$

$$= 27.7\,A - \frac{12\,V \cdot 7}{1.3\,\mu H \cdot 7^2 + 5\,\mu H} \cdot \frac{1 - 0.43}{2 \cdot 100\,kHz} = 24.3\,A$$

$$I_{SEC-peak} = \frac{I_{LV}}{2} + \frac{\Delta I_{Lo}}{2} = \frac{300\,A}{2} + \frac{75\,A}{2} = 187.5\,A$$

$$I_{SEC-valley} = \frac{I_{LV}}{2} - \frac{\Delta I_{Lo}}{2} = \frac{300\,A}{2} - \frac{75\,A}{2} = 112.5\,A \tag{11}$$

$$I_{SEC-valley2} = I_{SEC-peak} - \frac{V_{LV}}{L_O} \cdot \frac{1 - D}{2 \cdot F_{SW}} = 187.5\,A - \frac{12\,V}{1.3\,\mu H} \cdot \frac{1 - 0.43}{2 \cdot 100\,kHz} = 162\,A$$

where the suffix 2 designates the valley current at the end of the freewheeling interval of the primary MOSFETs, just before a diagonal pair of MOSFETs conducts.

## Practical Implementation

Fig. 6 shows a photo of a practical implementation of the proposed regulator design. It consists of a main board and two gate-driver daughterboards for the isolated primary gate driver and bipolar (15 V and −4 V) power

supply. The gate-driver daughterboards optimize contact lengths between power supplies and gate-driver secondary circuits for reduced routing complexity.



*Fig. 6. Photo of the bidirectional dc-dc regulator implementation.*

A current-sense transformer with a 100-to-1 turns ratio located close to the main transformer provides primary-side current sensing for peak current-mode control. Four MOSFETs connect in parallel on each leg of the current-doubler secondary. All MOSFETs connect to the bottom-side heat sink through a 4-mm thermal pad, and a high-current busbar mounts on the back side of the board between the synchronous rectifier MOSFETs and the negative bus terminals. A set of four paralleled 0.5-mΩ shunt resistors connected between the coupled inductor and the positive bus terminals facilitates measurement of the dc bus current on the low-voltage side.

## Performance Results

Moving on to the practical implementation, I measured the efficiency of the APM with 400-V and 12-V battery conditions and a load current up to 300 A. The peak efficiency was around 95.5%. Figs. 7 and 8 show the measured pole voltages, $V_A$ and $V_B$, at 10-A and 100-A loads. Fig. 9 shows the startup and load transient response.
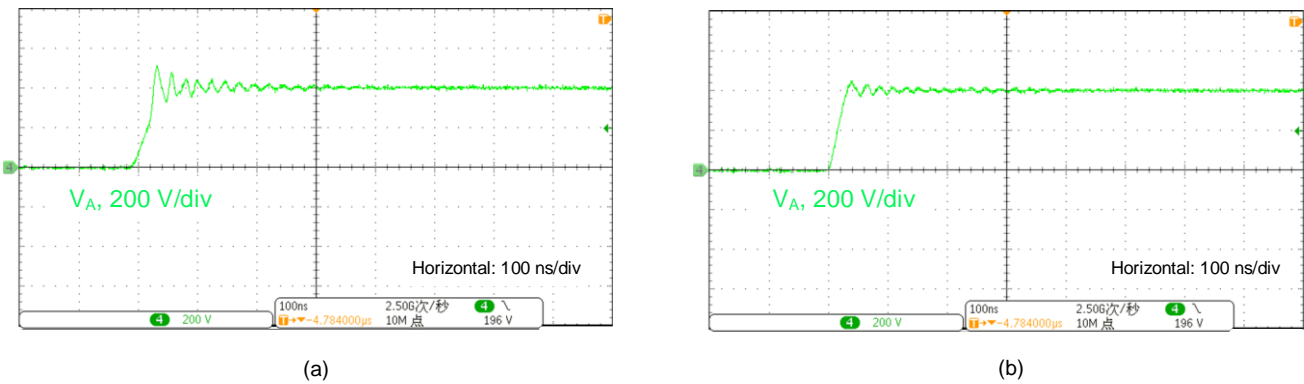


(a)



(b)

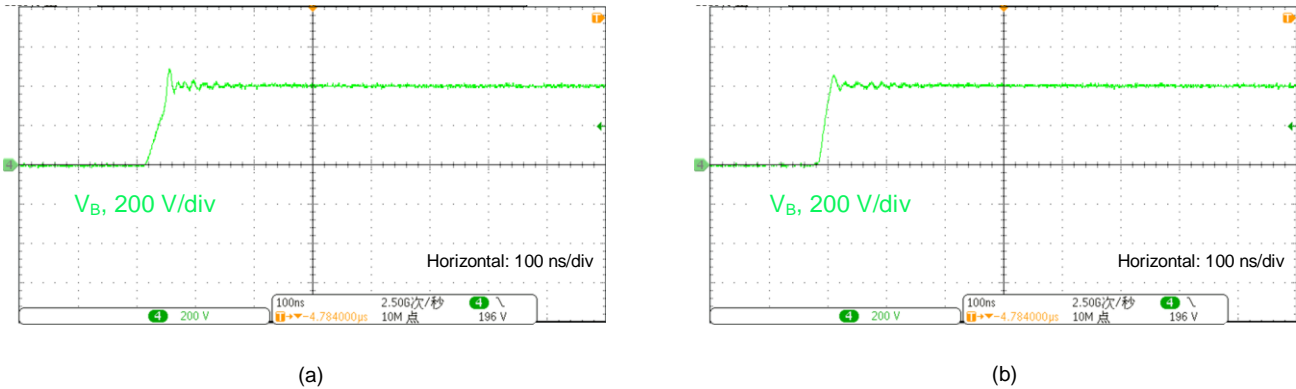*Fig. 7. Lagging-leg pole voltage at 10 A (a) and 100 A (b).*

(a)

(b)

*Fig. 8. Leading-leg pole voltage at 10 A (a) and 100 A (b).*
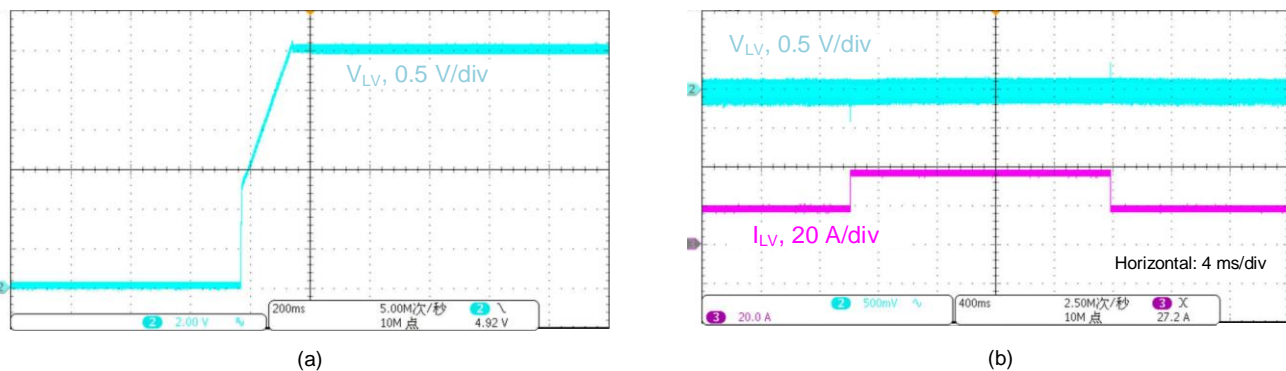


(a)

(b)

*Fig. 9. Startup (a) and 20-A load-step response (b).*

## Summary

My primary objective for this article was to describe, from a designer's perspective, the development flow of an APM that interfaces between the traction and auxiliary batteries, detailing an isolated PSFB dc-dc regulator with a current-doubler secondary, digital control enabling bidirectional capability, and functional safety assessed up to ASIL D. While digital control simplifies the implementation of bidirectional solutions, a unidirectional step-down regulator is possible using an analog PSFB controller. Reference designs are available for both scenarios to help designers implement similar circuits.

## References

1. "A Guide To Power Electronics Design For Off-Battery Automotive (Part 1): EMC And Line Transient Requirements" by Timothy Hegarty, How2Power Today, May 2022.

2. "A Guide To Power Electronics Design For Off-Battery Automotive (Part 2): DC-DC Conversion From 12 V" by Timothy Hegarty, How2Power Today, June 2022.

3. "A Guide To Power Electronics Design For Off-Battery Automotive (Part 3): DC-DC Conversion From 48 V" by Timothy Hegarty, How2Power Today, October 2022.

4. "Trends in Electric Light-Duty Vehicles—Global EV Outlook 2022," International Energy Agency (IEA), Accessed on Oct. 15, 2022.

5. "A Comprehensive Study of Implemented International Standards, Technical Challenges, Impacts and Prospects for Electric Vehicles" by Salman Habib, Muhammad Mansoor Khan, Farukh Abbas, Lei Sang, Muhammad Umair Shahid, and Houjun Tang, IEEE Access 6 (March 2018): pp. 13866-13890.

6.  "Electrical characteristics and electrical safety of high-voltage components in road vehicles." LV 123, German automotive OEMs.

7.  "Electrically propelled road vehicles – Electrical specifications and tests for voltage class B systems and components – Part 2: Electrical tests for components," ISO 21498-2, Edition 1, Geneva, Switzerland, March 2021.

8.  "Road Vehicles – Electrical disturbance by conduction and coupling – Part 4: Electrical transient conduction along shielded high voltage supply lines only," ISO/TS 7637-4, Edition 1, Geneva, Switzerland, May 2020.

9.  "Electric and hybrid electric road vehicles – Radio disturbance characteristics – Limits and methods of measurement for the protection of off-board receivers below 30 MHz," CISPR 36, Edition 1, Geneva, Switzerland, July 2020.

10. "Uniform provisions concerning the approval of vehicles with regard to specific requirements for the electric power train," UNECE Regulation No. 100, Revision 3, Geneva, Switzerland, March 2022.

11. "Keeping safe on the roads: series of standards for vehicle electronics functional safety just updated" by Clare Naden, ISO blog post, Dec. 19, 2018.

12. "ASIL D Safety Concept-Assessed High-Speed Traction, Bi-Directional DC/DC Conversion Reference Design," Texas Instruments reference design No. TIDM-02009, accessed Oct. 27, 2022.

13. "Automotive 400-V Battery to 12-V, 3.6-kW DC/DC Converter Reference Design," Texas Instruments reference design No. TIDA-020031, accessed Oct. 27, 2022.

14. "Phase Shifted Full Bridge (PSFB) vs. Full Bridge LLC (FB-LLC) for High Power DC/DC Conversion," Texas Instruments training video series, May 7, 2018.

15. "1kW, 400V/12V High Step-Down DC/DC Converter: Comparison Between Phase-Shifted Full-Bridge and LLC Resonant Converters," IEEE Transportation Electrification Conference and Expo (ITEC) (June 22-24, 2017): pp. 275-280.

16. "Optimal Dead-Time Control Scheme for Extended ZVS Range and Burst-Mode Operation of Phase-Shift Full-Bridge (PSFB) Converter at Very Light Load" by Chong-Eun Kim, IEEE Transactions on Power Electronics 34, no. 11 (November 2019): pp. 10823-10832.

17. "Onboard Charging DC/DC Converter of Electric Vehicle Based on Synchronous Rectification and Characteristic Analysis" by Haijun Tao, Guopeng Zhang, and Zheng Zheng, Journal of Advanced Transportation (June 2019): pp. 1-10.

18. "Optimization of a self-driven current-doubler phase shifted full bridge DC-DC converter with integrated magnetic" by Sevilay Cetin, Journal of Engineering Research 2, no. 4 (December 2014): pp. 47-65.

19. "A High-Performance, Integrated Powertrain Solution: The Key to EV Adoption" by Nagarajan Sridhar, Texas Instruments white paper, literature No. SLIY008, April 2021.

20. "Achieving High Efficiency and Enabling Integration in EV Powertrain Subsystems Using C2000 Real-Time MCUs" by Manish Bhardwaj and Wagar Mehmood, TI white paper, literature No. SWAY033, December 2020.

## About The Author

*Timothy Hegarty is a senior member of technical staff (SMTS) in the Buck Switching Regulators business unit at Texas Instruments. With over 25 years of power management engineering experience, he has written numerous conference papers, articles, seminars, white papers, application notes and blogs. Tim's current focus is on enabling technologies for high-frequency, low-EMI, isolated and nonisolated regulators with wide input voltage range, targeting industrial, communications and automotive applications in particular. He is a senior member of the IEEE and a member of the IEEE Power Electronics, Industrial Applications and EMC Societies.*

For more on power conversion in automotive applications, see the How2Power *Design Guide*, locate the Application category and select "Automotive".